ROYAL SOCIETY
OF CHEMISTRY

PAPER

Self-assembly of paramagnetic amphiphilic copolymers for synergistic therapy†

Zhiliang Gao,‡[a] Weiwei Mu,‡[b] Yuan Tian,[a] Yimao Su,[a] Huanli Sun, [ID][c]
Gaorui Zhang,[d] Anning Li,[d] Dexin Yu,[d] Na Zhang,[b] Jingcheng Hao, [ID][a]
Yongjun Liu*[b] and Jiwei Cui [ID] *[ae]

Engineering nanoparticles (NPs) with multifunctionality has become a promising strategy for cancer theranostics. Herein, theranostic polymer NPs are fabricated via the assembly of amphiphilic paramagnetic block copolymers (PCL-b-PIEtMn), in which IR-780 and doxorubicin (DOX) were co-encapsulated, for magnetic resonance (MR) and near infrared fluorescence (NIRF) imaging as well as for photo thermal therapy (PTT)-enhanced chemotherapy. The synthesized amphiphilic paramagnetic block copolymers demonstrated high relaxivity (r_1 = 7.05 mM^{-1} s^{-1}). The encapsulated DOX could be released with the trigger of near infrared (NIR) light. In vivo imaging confirmed that the paramagnetic NPs could be accumulated effectively at the tumor sites. Upon the NIR laser irradiation, tumor growth was inhibited by PTT-enhanced chemotherapy. The advantages of the reported system lie in the one-step convergence of multiple functions (i.e., imaging and therapy agents) into a one delivery vehicle and the dual mode imaging-guided synergistic PTT and chemotherapy. This study represents a new drug delivery vehicle of paramagnetic NPs for visualized theranostics.

Introduction

Theranostic nanoparticles (NPs) can encapsulate diagnostic and therapeutic agents for diagnosis and treatment of diseases.[1–7] Magnetic resonance imaging (MRI) is one of the most powerful techniques for tumor imaging due to its high contrast resolution for soft tissues, non-ionizing radiation, and multiplanar imaging.[8–10] Gadolinium (Gd)-based chelator complexes (e.g., Magnevist® and Omniscan™) are the widely used clinical MR contrast agents.[11–13] Recently, metallic oxides and transition metal complexes have been developed to improve MRI sensitivity and increase the contrast of the imaging sites from the background.[13–18] However, most of the reported contrast agents are limited to inorganic NPs or transition metal complexes, which potentially have some hepatorenal toxicity.[11,19] Therefore, it is necessary to develop biocompatible functional contrast agents.

Polymer NPs (e.g., polymer micelles, polymersomes, polymer–drug conjugates, and dendrimers) have been widely used as therapeutic carriers due to their biocompatibility, biodegradability, controlled drug encapsulation and release.[20–22] Therefore, it is desirable to engineer polymer NPs loaded with diagnostic reagents (e.g., MRI agents) and therapeutics for theranostics. The self-assembly of amphiphilic polymers based on hydrophobic inter-actions is one of the most commonly used methods to fabricate polymer NPs.[23–26] Hydrophobic therapeutic and diagnostic agents can be effectively encapsulated in the hydrophobic core of polymer NPs.[27–29] Hydrophobic dyes have been loaded in polymer NPs for fluorescence imaging.[30–32] However, polymer NPs for MRI are rarely reported since MR contrast agents are typically hydrophilic and thus difficult to be loaded inside polymer NPs. To prepare MRI-based polymer NPs, MRI contrast agents need to be modified at the hydrophilic region of the NPs. Therefore, synthesis and self-assembly of paramagnetic amphiphilic block copolymers are potentially used for engineering polymer NPs for MRI. In addition, the ability of macromolecule contrast agents for a short long-itudinal (T_1) relaxation time of the surrounding water protons was stronger than the small molecule contrast agents.

Although chemotherapy has been widely used for cancer treatment, it is usually limited by its severe side effects and low

[a] Key Laboratory of Colloid and Interface Chemistry of the Ministry of Education, School of Chemistry and Chemical Engineering, Shandong University, Jinan, Shandong 250100, China. E-mail: jwcui@sdu.edu.cn

[b] Key Laboratory of Chemical Biology of the Ministry of Education, School of Pharmaceutical Sciences, Shandong University, Jinan, Shandong 250012, China. E-mail: liuyongjun@sdu.edu.cn

[c] Jiangsu Key Laboratory of Advanced Functional Polymer Design and Application, College of Chemistry, Chemical Engineering and Materials Science, Soochow University, Suzhou, Jiangsu 215123, China

[d] Department of Radiology, Qilu Hospital, Shandong University, Jinan, Shandong 250012, China

[e] State Key Laboratory of Microbial Technology, Shandong University, Qingdao, Shandong 266237, China

† Electronic supplementary information (ESI) available. See DOI: 10.1039/d0tb00405g

‡ These authors contributed equally to this work.

utilization efficiency.[33–35] Many hydrophobic drugs (*e.g.*, doxorubicin (DOX), paclitaxel, and hydroxycamptothecin) have high activity but are difficult to deliver using conventional formulation techniques.[36] Polymer micelles with a hydrophobic core and a hydrophilic shell provide a versatile approach for the delivery of hydrophobic drugs. However, the controllable release of hydrophobic drugs is still challenging.[37] Various stimuli, including pH, thermal, redox, and light, have been developed for the controlled release of anticancer drugs.[37–41] In addition, synergistic therapy is a feasible strategy to improve treatment efficacy.[42] Near infrared (NIR) light irradiation has large penetration depth, high photothermal (PT) efficacy, and low tissue damage. Thus, NIR-activated PTT associated with enhanced chemotherapy is of particular interest in the realm of cancer therapy. Upon NIR irradiation, the laser is transduced into local heat by the PT agents, which then enhances the release of drugs from the core of polymer NPs.[43,44] Furthermore, the rise in temperature due to the PT agents can also directly increase toxicity to cancer cells.[26,45]
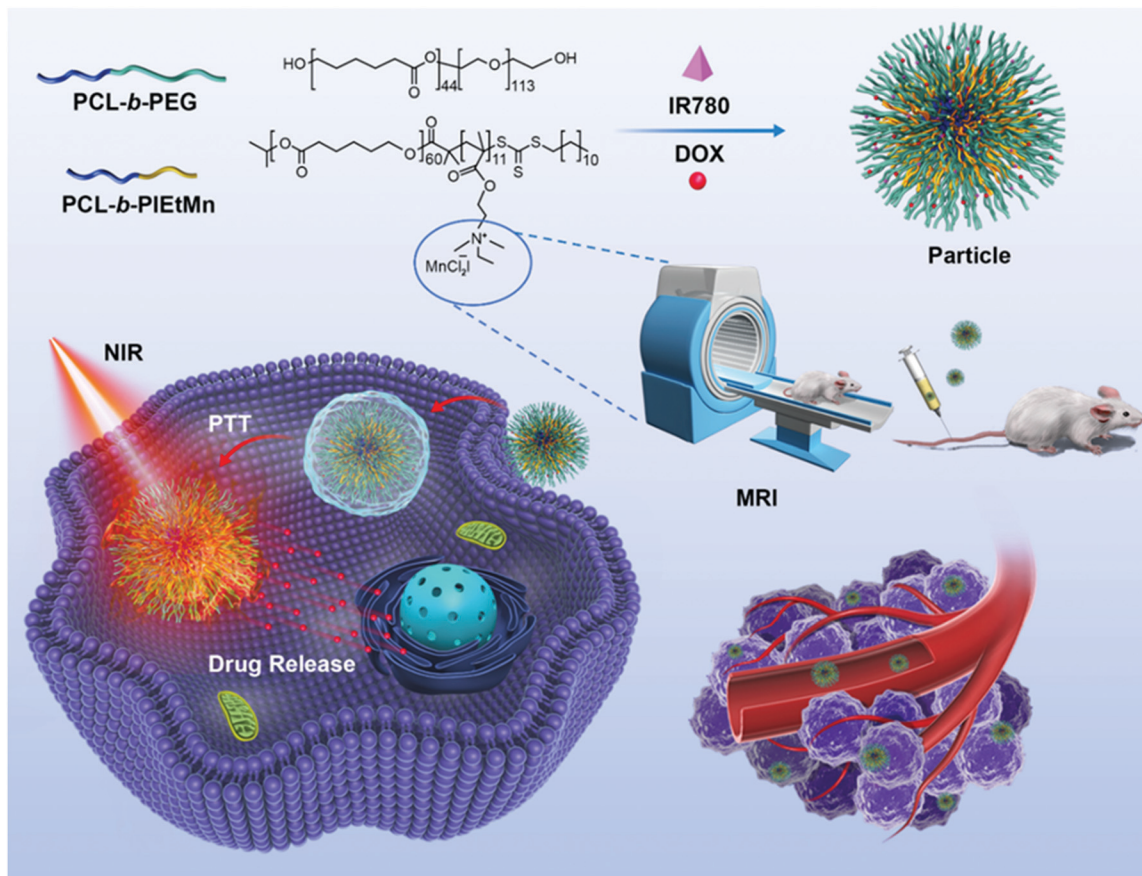
Herein, we assembled paramagnetic polymer NPs loaded with DOX and IR-780 for dual mode imaging (*i.e.*, fluorescence and MRI) and PTT-enhanced chemotherapy (Scheme 1). The paramagnetic block polymer with Mn^{2+} as counter ions not only acted as a component for the assembly of polymer NPs, but also served as a MRI contrast agent. DOX and IR-780 were co-encapsulated in the core of polymer NPs based on hydrophobic interactions. The co-assembly of polycaprolactone-*b*-poly(ethylene glycol) (PCL-*b*-PEG) could effectively shield the positive charge of the paramagnetic polymer chains and thereby could prolong the blood circulation time and improve the accumulation of NPs at the tumor sites. Upon 808 nm NIR laser irradiation, the encapsulated IR-780 could transduce light into local heat to kill cancer cells and activate DOX release. Furthermore, IR-780 could also be applied for *in vivo* fluorescence imaging. More importantly, the paramagnetic polymer NPs with Mn^{2+} as counter ions could effectively shorten the longitudinal (T_1) relaxation time of the surrounding water protons and show high relaxivity ($r_1 = 7.05$ mM^{-1} s^{-1}). The as-prepared paramagnetic NPs demonstrated two distinct features: (i) the self-assembly of the paramagnetic polymer enables the one-step convergence of multiple functions (*i.e.*, imaging and therapy agents) into a one delivery vehicle and (ii) dual mode imaging-guided PTT can improve chemotherapy.

Results and discussion

Nanoengineering and characterization of paramagnetic polymer NPs

Amphiphilic block copolymers were synthesized using the reversible addition–fragmentation chain transfer (RAFT) polymerization

Scheme 1 Illustration of the preparation of paramagnetic NPs for cancer theranostics.

method, which included the synthesis of a macromolecular chain transfer agent, polycaprolactone-*b*-poly(2-(dimethylamino)-ethyl methacrylate) (PCL-*b*-PDMAEMA) block copolymer, quaternary ammoniation (PCL-*b*-PIEt), and coordination with Mn^{2+} (PCL-*b*-PIEtMn) (Fig. S1, ESI†). Proton nuclear magnetic resonance (^{1}H NMR) spectra demonstrated the successful synthesis of the amphiphilic block copolymer (Fig. S2, ESI†). The magnetic properties of amphiphilic block copolymers were studied using the SQUID method. As shown in Fig. 1a, the PCL-*b*-PIEtMn block copolymer showed a linear relationship between magnetization (M) and magnetic field (H), which indicated that the copolymer was a paramagnetic material.[46–48] PCL-*b*-PEG was used to co-assemble with PCL-*b*-PIEtMn for the fabrication of NPs, in which the longer PEG chain could shield the positive charge of the paramagnetic block (Fig. S3, ESI†). The molar ratio of the two block copolymers could influence the size of the NPs. As shown in Fig. 1b, the amount of paramagnetic block copolymer had negligible influence on the hydrodynamic diameter ($\sim$150 nm) when the mass ratio of PCL-*b*-PEG and PCL-*b*-PIEtMn was below 1:1. However, the average hydrodynamic diameter of paramagnetic NPs increased from about

200 to 350 nm when the mass ratio of PCL-*b*-PEG and PCL-*b*-PIEtMn changed from 1:2 to 1:3. To make the NPs contain more paramagnetic polymer components for MRI and have a suitable particle size for therapeutic delivery, the mass ratio of 1:1 was chosen for further studies. The longitudinal proton relaxation time (T_1) of paramagnetic NPs was examined using a 3.0 T MR scanner to investigate the potential application for MRI. The T_1 relaxation rate of water protons increased and therefore led to an increase of the water MRI signal in a T_1-weighted image, which caused an increase of the MRI contrast (Fig. 1c). According to the linear fitting results, the r_1 relaxivity of paramagnetic NPs was 7.05 mM^{-1} s^{-1}, which could effectively shorten the longitudinal (T_1) relaxation time and increase the MRI contrast to the background. To test the stability, the assembled NPs were incubated with Dulbecco's Phosphate-Buffered Saline (DPBS, 10 mmol, pH 7.4) and a cell culture medium, respectively, for seven days. The hydrodynamic diameter maintained 150 nm before and after incubation, which suggested the good stability of NPs (Fig. S4, ESI†). During assembly, both DOX and IR-780 could be encapsulated into the NPs, which was proved by UV-vis spectroscopy and the color appearance of the
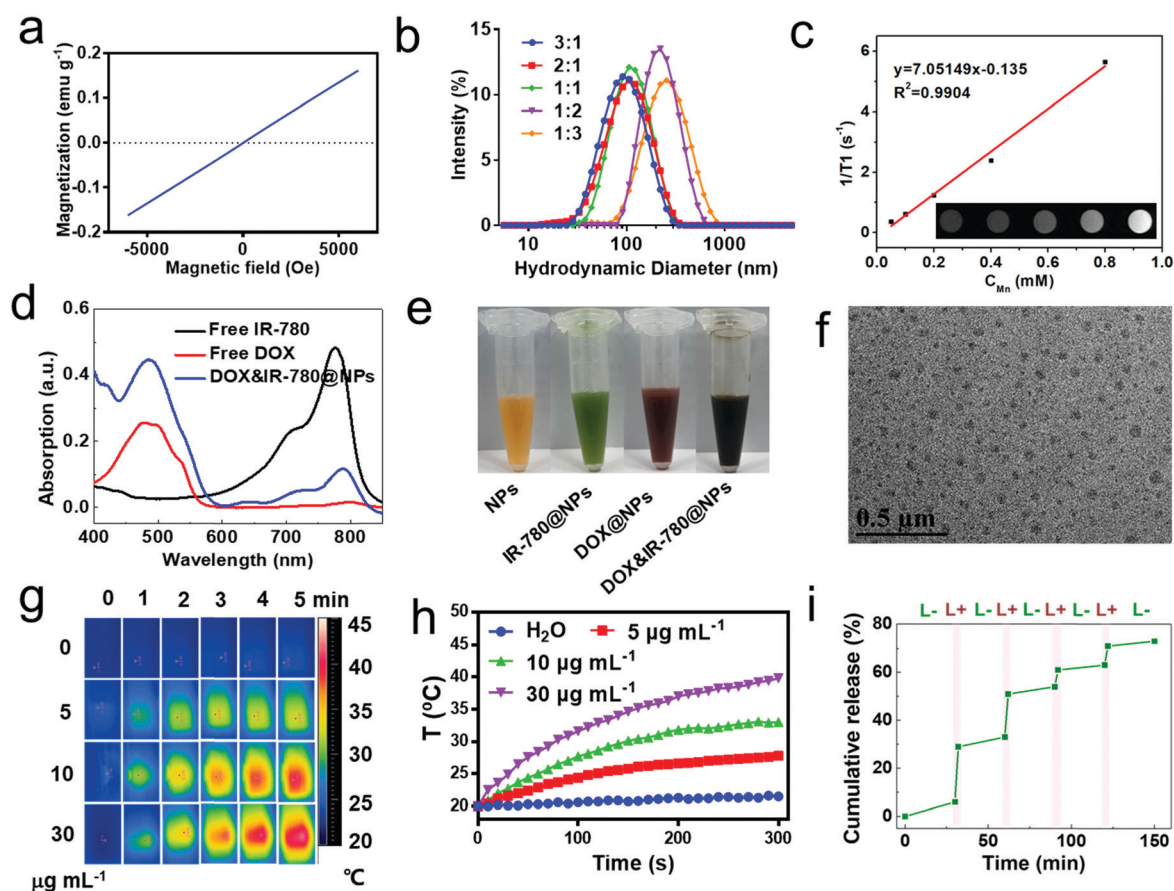

Fig. 1 (a) SQUID magnetometry of paramagnetic block copolymer (PCL-*b*-PIEtMn). (b) Hydrodynamic diameter of NPs with different mass ratios of PCL-*b*-PEG and PCL-*b*-PIEtMn. (c) Relaxivity measurements of the PCL-*b*-PIEtMn NP suspension. The r_1 relaxivity was obtained from fitting the slope of the samples. The inset is T_1-weighted MR images of PCL-*b*-PIEtMn solutions measured at 3.0 T. (d) UV-vis absorption spectra of IR-780, DOX, and DOX&IR-780@NPs. (e) Photographs of different paramagnetic NP suspensions. (f) Transmission electron microscopy (TEM) image of paramagnetic NPs. (g) Photothermal pictures of DOX&IR-780@NPs under 808 nm NIR irradiation. (h) Temperature monitoring during the photothermal process (power density: 0.5 W cm^{-2}). (i) DOX release profiles from DOX&IR-780@NPs with four laser off/on cycles (power density: 0.5 W cm^{-2} and laser irradiation time: 5 min).

NP suspension (Fig. 1d and e). The loading amounts of DOX and IR-780 were 5.3% and 2.0%, respectively (Fig. S5, ESI†). In addition, the cargo loading did not influence the size distribution and dispersity (Fig. 1f). Polymer NPs loaded with DOX, IR-780, and both DOX and IR-780 were abbreviated as DOX@NPs, IR-780@NPs and DOX&IR-780@NPs, respectively.

Photothermal and photoswitchable drug release

To examine the photothermal behavior of DOX&IR-780@NPs, temperature changes during the laser irradiation process were monitored using an infrared camera. As shown in Fig. 1g and h, a concentration dependent photothermal behavior was observed. At the concentration of 30 $\mu g\ mL^{-1}$, the temperature increase is about 20 $^\circ$C after 5 min irradiation. Such a temperature increase of the NP suspension could lead to irreversible damage of tumor cells.[49,50] As a control, the temperature of water after 5 min of irradiation did not significantly change. These results indicated that DOX&IR-780@NPs could be potentially used for PTT. The NIR-triggered drug release behavior was also investigated. Under the NIR irradiation at 808 nm (1.0 W cm^{-2}, 5 min), a burst release of DOX was observed (Fig. 1i). After 4 cycles of NIR laser irradiation (1.0 W cm^{-2}, 5 min), about 70% of DOX was

released from DOX&IR-780@NPs. More interestingly, the DOX release could be held by tuning off the NIR irradiation. Therefore, the release of DOX from NPs can be conveniently controlled by the NIR laser "on" and "off" cycles, which can be explained by a diffusion-controlled release. Upon 808 nm laser irradiation, the light energy was converted into local heat by IR-780, which led to the phase transition of the PCL core. The melting of the PCL core could increase water penetration into the hydrophobic domain and decrease the stability of NPs, which resulted in enhanced drug diffusion from NPs to the dispersion solution.[37,43,51]

Cell association and *in vitro* cytotoxicity

Cell association and NIR-activated intracellular drug release were studied by flow cytometry and confocal laser scanning microscopy (CLSM), respectively. As shown in Fig. 2a, cells incubated with DOX&IR-780@NPs exhibited stronger fluorescence compared to free DOX, which demonstrated that NPs enhanced the DOX delivery into cells through endocytosis.[37] More importantly, the fluorescence intensity of cells incubated with DOX&IR-780@NPs L+ (laser on) was higher than that of the DOX&IR-780@NPs L− (laser off). The possible reason for
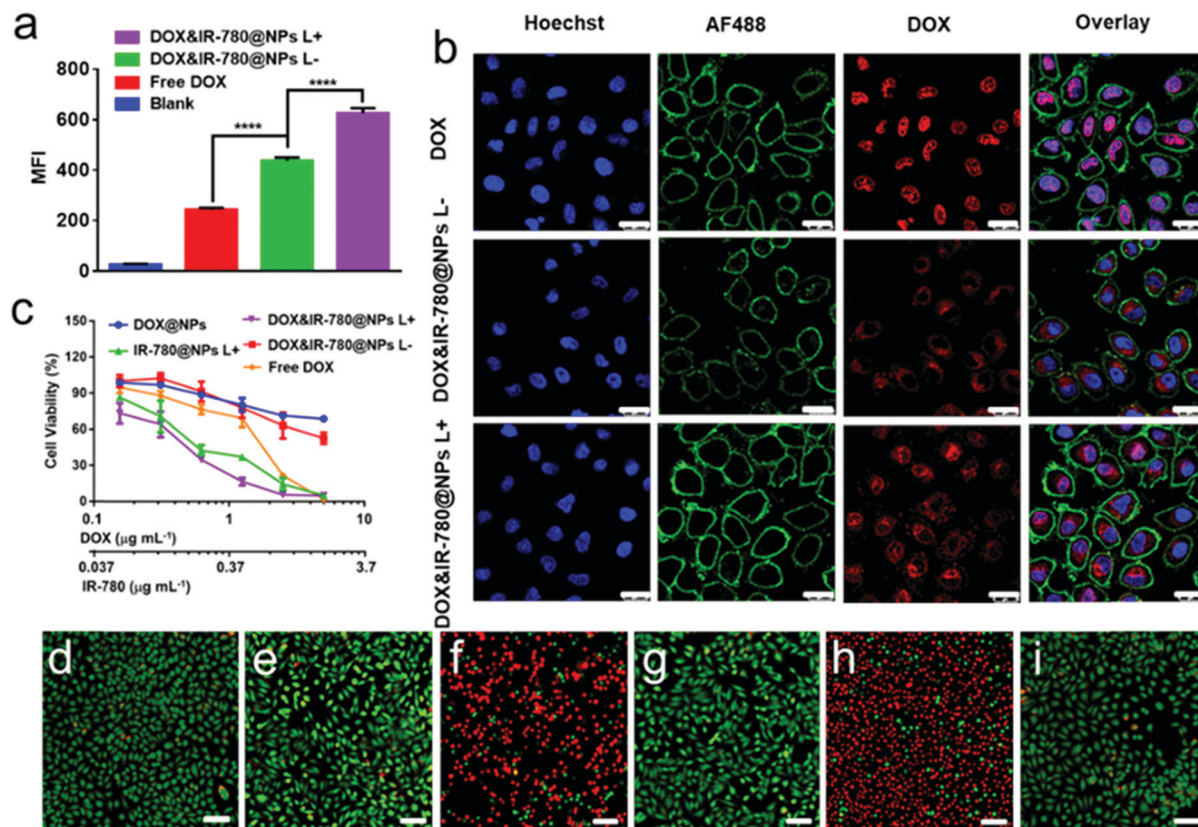

Fig. 2 (a) Cellular uptake of free DOX, DOX&IR-780@NPs L−, and DOX&IR-780@NPs L+ (DOX concentration: 5 $\mu g\ mL^{-1}$) of MCF-7 cells (mean ± SD, $n = 3$, ****$p < 0.0001$). (b) CLSM images of MCF-7 cells after incubation for 4 h with free DOX or DOX&IR-780@NPs (L−: laser off, L+: laser on for 5 min, DOX concentration: 5 $\mu g\ mL^{-1}$). Hoechst (blue) and wheat germ agglutinin Alexa Fluor 488 conjugate (green) were used to stain the cell nuclei and membrane, respectively. Scale bars are 10 μm. (c) MCF-7 cell viability of DOX, DOX@NPs, IR-780@NPs L+, DOX&IR-780@NPs L−, and DOX&IR-780@NPs L+ after 48 h incubation (mean ± SD, $n = 3$). Live/dead assay of MCF-7 cells after incubation with (d) cell medium only, (e) DOX, (f) IR-780@NPs L+, (g) DOX@NPs, (h) DOX&IR-780@NPs L+, and (i) DOX&IR-780@NPs L− for 12 h. Equivalent DOX concentration was 5 $\mu g\ mL^{-1}$. Scale bars are 50 μm.

this is that fluorescence is partially quenched when DOX is encapsulated into NPs, and the released DOX from NPs improves the fluorescence intensity.[43,52,53] In addition, CLSM was also used to investigate the cell uptake of NPs. As shown in Fig. 2b and Fig. S6, ESI,† a red fluorescence signal was observed in the cell nuclei after incubation with free DOX. When the cells were incubated with DOX&IR-780@NPs without NIR irradiation, DOX signals were mainly localized in the cell cytoplasm near the nuclei. However, stronger DOX signals were observed in the cell nuclei when the cells were incubated with DOX&IR-780@NPs after NIR irradiation, which indicated that NIR helped the intracellular DOX release and translocation to the

nuclei. The cross-sectional images of MCF-7 cells could also demonstrate that DOX was translocated in the cell nuclei (Fig. S7, ESI†).

In vitro cytotoxicity of the NPs was evaluated with MCF-7 cells using an ATPLite-based assay. The cytotoxicity of NPs without cargo loading was negligible even after 48 h incubation at a NP concentration of 500 μg mL^{-1} (Fig. S8, ESI†). After NIR irradiation at 808 nm, cell viability of NPs loaded with IR-780 regardless of DOX encapsulation decreased significantly along with increasing sample concentration (Fig. 2c), which demonstrated that the PTT played a dominant role in cytotoxicity *in vitro*. It should be noted that free DOX exhibited higher
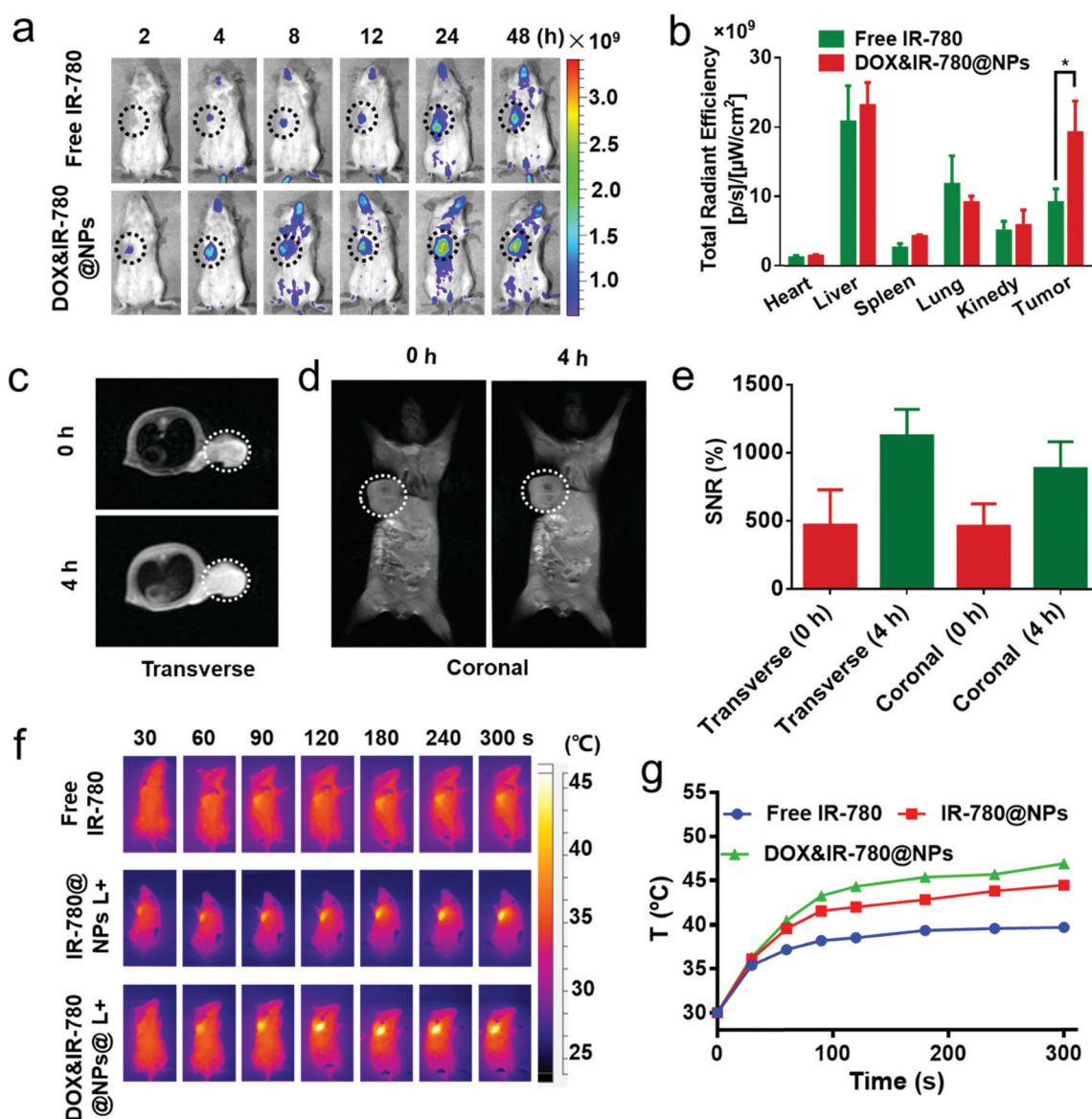

Fig. 3 (a) *In vivo* fluorescence imaging of the 4T1 tumor-bearing mice after intravenous injection of free IR-780 or DOX&IR-780@NPs at 2, 4, 8, 12, 24, 48 h, respectively. (b) Quantification of IR-780 intensities of different organs and tumors from *ex vivo* evaluation (*$p < 0.5$). (c and d) *In vivo* T_1-weighted MR images of 4T1 tumor-bearing mice before and after intravenous injection of DOX&IR-780@NPs at 4 h. (c) Transverse position and (d) coronal position. (e) Quantification of the signal-to-noise ratio (SNR) at the tumor site before and after intravenous injection of DOX&IR-780@NPs at 4 h. Photothermal images (f) and temperature monitoring (g) of tumors after intravenous injection of free IR-780, IR-780@NPs L+, or DOX&IR-780@NPs L+ for 24 h. Data are presented as mean ± SD ($n = 3$).

cytotoxicity than the DOX@NPs and DOX&IR-780@NPs L− due to the slow release of DOX from the NPs. In addition, the live/dead assay further confirmed the synergistic therapy, where the live and dead cells were stained with Calcein-AM (green fluorescence) and propidium iodide (PI, red fluorescence), respectively. The groups of IR-780@NPs L+ and DOX&IR-780@NPs L+ resulted in 95% cell death, while negligible cell death was observed in other groups (cell medium, DOX, DOX@NPs, and DOX&IR-780@NPs L− groups), which further confirmed the dominate role of PTT in cytotoxicity according to the ATPLite-based assay (Fig. 2d–i).

In vivo imaging and biodistribution

To demonstrate the capacity of in vivo dual mode imaging of DOX&IR-780@NPs, NIRF imaging and T_1-weighted MRI were performed on 4T1 tumor-bearing mice. After intravenous injection of DOX&IR-780@NPs and free IR-780, mice were monitored by NIRF at the predetermined time. NPs gradually accumulated at the tumor site and exhibited the highest tumor accumulation at 24 h post-injection (Fig. 3a). To analyze the biodistribution of NPs, the main organs and tumors of mice were harvested at 12, 24, and 48 h post-injection. NIRF images and quantitative analysis demonstrated that NPs showed higher tumor accumulation compared to free IR-780 at 24 h post-injection (Fig. 3b and Fig. S9, S10, ESI†). MRI was also performed to investigate the in vivo biodistribution of paramagnetic NPs. After intravenous injection of DOX&IR-780@NPs, MRI images were obtained after 4 h and the brightness contrast of the tumor site was higher compared to that without the

injection of paramagnetic NPs (Fig. 3c and d). The MRI signal intensities of the tumor with and without injection of DOX&IR-780@NPs were quantitatively calculated (Fig. 3e). Both signals at the transverse position and coronal position were enhanced 2.3- and 1.8-fold, respectively, compared to the control group without the injection of NPs.

According to the in vivo fluorescence imaging, the maximum NP accumulation at the tumor site was at 24 h (Fig. 3a), which was selected as the time point for PT measurements. After the intravenous injection of DOX&IR-780@NPs, IR-780@NPs, or free IR-780, the tumor sites were irradiated with 808 nm NIR laser (1.0 W cm^{-2}) for 5 min and the temperature was monitored using an IR thermal camera (Fig. 3f). The temperature of the tumor sites increased rapidly and was maintained at 47 °C and 45 °C for the groups injected with DOX&IR-780@NPs and IR-780@NPs, respectively. However, the injected free IR-780 only induced a minor temperature increase (~8 °C) after 5 min irradiation (Fig. 3g). The possible reason is that the NPs had higher accumulation at the tumor sites compared to free IR-780.

In vivo antitumor efficacy

PBS, free DOX, free IR-780 L+, DOX@NPs, IR-780@NPs L+, DOX&IR-780@NPs L−, or DOX&IR-780@NPs L+, were injected to examine the PTT on 4T1 tumor-bearing mice. Tumor sites were irradiated with 808 nm NIR laser at 24 h post-injection. As shown in Fig. 4a and b, except for the PBS group, all the other groups showed different levels of inhibition of tumor growth.
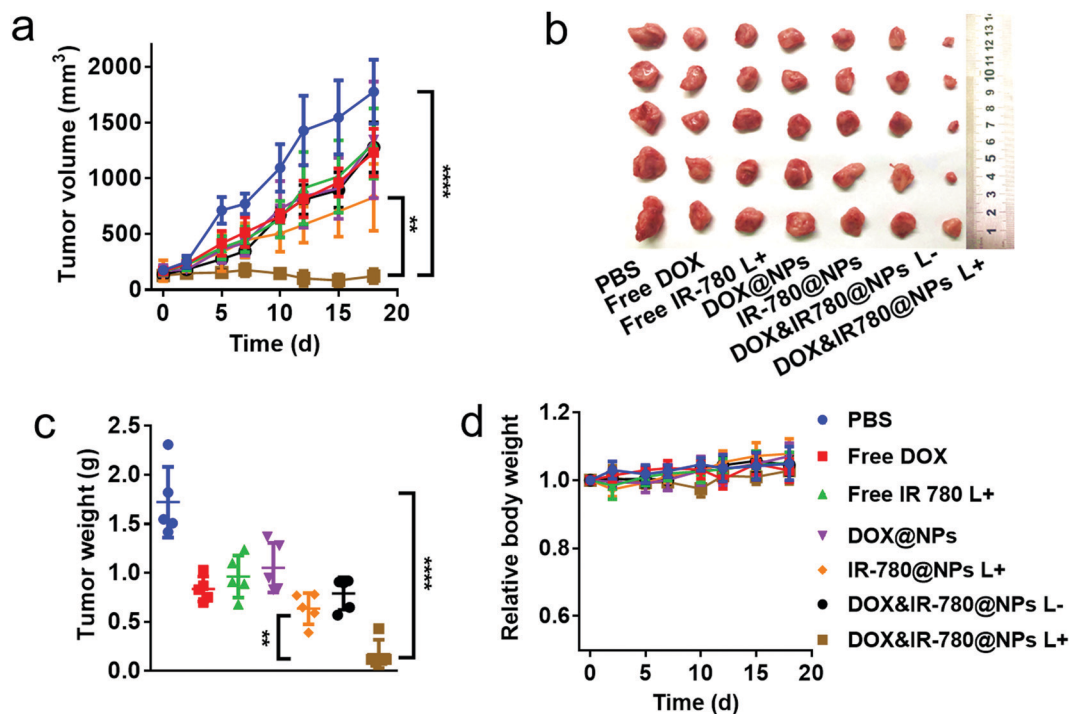

Fig. 4 (a) Tumor volume changes of 4T1 tumor–bearing mice after various treatments. Injections of various formulations were administered at 1, 3, and 7 days and the irradiation with an NIR laser was applied at 24 h after injection. Photograph (b) and tumor weight (c) of the harvested 4T1 tumors after 18 days of evaluation (**$p < 0.01$ and ****$p < 0.0001$). (d) Relative body weight of 4T1 tumor–bearing mice after various treatments. Data are presented as mean ± SD ($n = 5$).
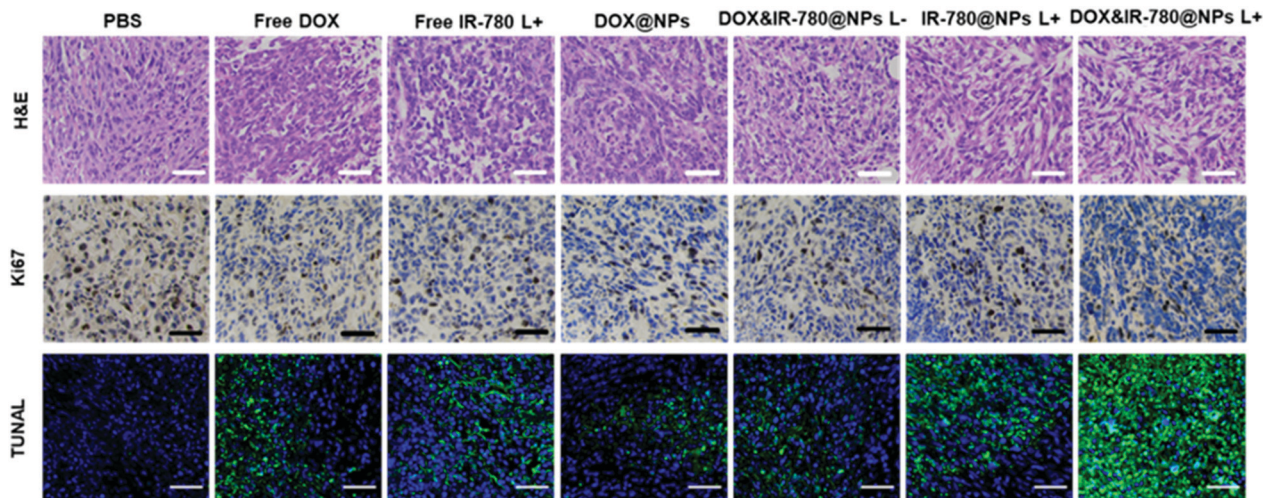
Fig. 5 H&E, Ki67 and TUNAL analyses of tumor tissues after treatment. Scale bars are 100 μm.

In particular, the DOX&IR-780@NPs L+ group resulted in the most significant tumor inhibition. The tumor weight from different groups also confirmed the corresponding therapeutic effects (Fig. 4c). From these results, either chemotherapy or PTT could partially but not efficiently inhibit tumor growth. PTT and chemotherapy (*i.e.*, DOX&IR-780@NPs L+ group) could show the synergetic effect and efficiently inhibit tumor growth. In addition, it was noted that the body weight of mice for all the groups had no significant changes during the treatment (Fig. 4d).

Hematoxylin and eosin (H&E) staining analysis of tumors was also examined to further evaluate the therapeutic effects. The DOX&IR-780@NPs L+ group showed much more tumor cell damage and tumor structure disruption than the other groups (Fig. 5). In addition, cell proliferation and apoptosis for tumor tissues were also analyzed using Ki67 and terminal deoxynucleotidyl transferase-mediated dUTP nick-end labeling (TUNEL) assays, respectively. As shown in Fig. 5, upon NIR laser irradiation, DOX&IR-780@NPs could effectively inhibit the proliferation of cancer cells and cause significant cancer cell apoptosis, compared to the other groups. Importantly, the paramagnetic NPs did not induce obvious damage to the normal tissues, including the heart, liver, spleen, lungs, and kidneys (Fig. S11, ESI†), which demonstrated the good biocompatibility of the NPs.

Conclusions

In summary, we reported a theranostic vehicle based on paramagnetic polymers for bio-imaging (*i.e.*, MR and NIRF imaging) and PTT-enhanced chemotherapy. DOX and IR-780 could be encapsulated in the paramagnetic NPs during the self-assembly of amphiphilic paramagnetic block copolymers. A controlled release of the encapsulated DOX was tuned using an 808 nm NIR laser. Both *in vitro* and *in vivo* experiments demonstrated the synergistic effect of PTT and chemotherapy. NIRF imaging indicated that maximum tumor accumulation of DOX&IR-780@NPs

was at 24 h post-injection. The paramagnetic NPs could dramatically shorten the longitudinal (T_1) relaxation time of the surrounding water protons for MRI, which indicated the potential of NPs for cancer diagnosis and visualization therapy. The reported paramagnetic NPs provide a new nanoplatform for visualized theranostics of cancer diagnosis and treatment.

Experimental section

Materials

DMAEMA, iodoethane, 2-methyl-2-[(dodecylsulfanylthio-carbonyl)-sulfanyl]propanoic acid (MDFC), triethylamine, 4-dimethylamino-pyridine, manganese(II) chloride and IR-780 were purchased from J&K Scientific Ltd (China). PCL$_{44}$-*b*-PEG$_{113}$ was obtained from Xi'an ruixi Biological Technology Co., Ltd (China). 1-(3-Dimethylamino-propyl)-3-ethylcarbodiimide hydrochloride (EDC) and 4-dimethyl-aminopyridine were obtained from Sigma-Aldrich (China). DOX and propidium iodide were bought from Aladdin (China). Hoechst 33342 and wheat germ agglutinin Alexa Fluor 488 conjugate (WGA-AF488) were obtained from Thermo Fisher Scientific (China). Calcein-AM was purchased from Dalian Meilun Biotech Co., Ltd (China). Dulbecco's modified Eagle medium (DMEM) and DPBS were bought from Neuronbc (China). Fetal bovine serum (FBS) and 0.5% Trypsin-EDTA were obtained from Gibco (Germany). The ATPlite luminescence assay system was obtained from PerkinElmer Co., Ltd (China). Ultrapure water was obtained using a Milli-Q system (Integral 5) with a resistivity of 18.2 MΩ cm.

Characterizations

^{1}H NMR spectra were recorded on a Bruker Avance 400 spectro-meter (Germany). Size and zeta potential of the NPs were measured using a Malvern Zetasizer Nano ZS90 instrument (England). TEM measurements were performed on a JEOL JEM-1400 TEM (Japan) at an operating voltage of 120 kV. The concentration of DOX was determined at 480 nm using a

UV-2600 UV-vis spectrometer. *In vitro* and *in vivo* photothermal behaviors were recorded using an IR thermal camera (Fluke, TiS75, USA). Cell imaging was performed using CLSM (Leica TCS SP8 STED 3X, Germany). Cytotoxicity measurements were performed on a plate reader (TECAN Spark 10M). Cell association was quantitatively determined by flow cytometry (ACEA NovoCyte 3009). MRI images were obtained on a 3.0 T MRI scanner (GE Signa HDx 3.0 T, USA). *In vivo* imaging and biodistribution were performed on an IVIS Spectrum imaging system (PerkinElmer, USA).

Synthesis of PCL-*b*-PIEtMn block copolymers

The PCL-*b*-PIEtMn copolymer was synthesized using a RAFT polymerization method, which is illustrated in Fig. S1, ESI.† Hydroxyl-terminal isopropyl polycaprolactone (PCL$_{60}$-OH) was synthesized as reported previously and the PDI of PCL$_{60}$-OH was 1.3.[54] For the synthesis of macromolecular chain transfer agent PCL-MDFC, MDFC (109.3 mg, 0.3 mmol), PCL-OH (350 mg, 0.1 mmol), EDC (77.35 mg, 0.4 mmol), and DMAP (48.87 mg, 0.4 mmol) were dissolved in 10 mL of dichloromethane and stirred at 25 °C for 24 h. After the reaction, the mixture was precipitated with 200 mL of diethyl ether. The precipitation was collected by centrifugation and purified twice by recrystallization with dichloromethane and diethyl ether. The final product was obtained as a yellow powder (332.3 mg, 86%). ^{1}H NMR (400 MHz, CDCl$_3$, (Fig. S2, ESI†)): δ (ppm) = 1.22–1.31 (19 H, CH_3(CH_2)$_{10}$), 2.27–2.38 (123 H, OCOCH_2C H_2), 4.00–4.13 (121 H, OCH_2CH$_2$CH$_2$).

The PCL-*b*-PDMAEMA block copolymer was synthesized using a RAFT polymerization method. In brief, PCL-MDFC (177.8 mg, 0.025 mmol), DMAEMA (117.9 mg, 0.75 mmol), and 2,2′-azobis(2-methylpropionitrile) (AIBN) (8.22 mg, 0.05 mmol) were dissolved in *N*,*N*-dimethylformamide (DMF) (2 mL) in a 25 mL Schlenk flask and deoxygenated by three freeze–pump–thaw cycles, followed by stirring at 90 °C for 24 h. Finally, the mixture was precipitated with cold diethyl ether and dried under vacuum. The final product was obtained as a white powder (110.86 mg, 61%), and the molecular weight was determined to be 8780 g mol^{-1} from ^{1}H NMR analysis. The polymerization degree of PDMAEMA was 11. ^{1}H NMR (400 MHz, CDCl$_3$, (Fig. S2, ESI†)): δ (ppm) = 2.45–2.65 (22H, OCH$_2$CH_2N), 4.00–4.13 (142 H, OCH_2CH$_2$CH$_2$, OCH_2CH$_2$).

The PCL-*b*-PIEtMn copolymer was synthesized by quaternization of PCL-*b*-PDMAEMA and complexation with iron.[47] Iodoethane (300 μL, 0.4 mmol) was dropwise added into the PCL-*b*-PDMAEMA (175.6 mg, 0.02 mmol) solution in 20 mL of dioxane, followed by stirring at 70 °C for 12 h. 20 mL of diethyl ether was added to precipitate the product. The product was centrifuged and dried under vacuum to obtain a yellow powder (144.75 mg, 81%). ^{1}H NMR (400 MHz, CDCl$_3$, (Fig. S2, ESI†)): δ (ppm) = 1.4–1.6 (33 H, NCH$_2$CH_3), 3.6–3.8 (44 H, NCH_2). For the synthesis of PCL-*b*-PIEtMn, PCL-*b*-PIEt (210 mg, 0.02 mmol) and MnCl$_2$·4H$_2$O (11.87, 0.06 mmol) were dissolved in 5 mL of water and then stirred at 25 °C for 24 h. Subsequently, the sample was dialyzed for 2 days to remove free manganese ions. The final product was freeze-dried to obtain the product.

Preparation of NPs

Paramagnetic polymer NPs were prepared using a co-solvent method.[55] Briefly, PCL-*b*-PIEtMn copolymers (5 mg) and PCL-*b*-PEG (5 mg) were dissolved in 1 mL of DMF, into which 9 mL of water was dropwise added using a syringe pump at a flow rate of 10 mL h^{-1} with vigorous stirring. The mixture was dialyzed with water for 2 days to remove DMF and concentrated to 1 mL by ultrafiltration (100 kDa). Hydrochloric acid on DOX was removed by mixing DOX (10 mg) with triethylamine (25 μL) in DMF (1 mL) for 12 h. The treated DOX solution in DMF (0.1 mL), IR-780 (0.5 mg), PCL-*b*-PIEtMn copolymer (5 mg), and PCL-*b*-PEG (5 mg) were dissolved in 0.9 mL of DMF and then 9 mL of water was dropwise added. The following processes were the same for the preparation of non-loaded NPs. The loading contents of DOX and IR-780 were 5.3% and 2.0%, respectively, based on the UV-vis analysis.

In vitro photothermal behavior

To assess the photothermal behavior, 1 mL of DOX&IR-780@ NPs in water with different IR-780 concentrations (5, 10, or 30 μg mL^{-1}) were irradiated with an 808 nm NIR laser (0.5 W cm^{-2}) for 5 min. The temperature of the solution was recorded using an infrared camera. Water was used as a control and irradiated under the same condition.

In vitro DOX release kinetics

The NIR-triggered drug release was monitored using UV-vis absorption spectra. 10 mL of DOX&IR-780@NP suspension (an equivalent DOX concentration of 50 μg mL^{-1}) in PBS (10 mM, pH 7.4) was irradiated with an NIR laser (0.5 W cm^{-2}) for 5 min at the predetermined time. After irradiation, 500 μL of suspension was taken out and ultrafiltrated subsequently for analysis.

Cell association

Cell association was investigated by incubating MCF-7 cells with DOX-loaded NPs. The MCF-7 cells were seeded into 24-well plates at a density of 5×10^4 cells per well and allowed to attach overnight. Subsequently, DOX-loaded NPs (an equivalent DOX concentration of 5 μg mL^{-1}) were incubated with the cells for 1, 2, and 4 h. After incubation, the cells were washed twice with DPBS and harvested by trypsinization. Subsequently, the cells were resuspended in 500 μL DPBS and analyzed with flow cytometry.

For cell imaging, MCF-7 cells were seeded in 14 mm confocal dishes with a density of 5×10^4 cells per well and cultured at 37 °C for 12 h. DOX and DOX-loaded NPs (an equivalent DOX concentration of 5 μg mL^{-1}) were incubated with MCF-7 cells for 4 h. For the DOX&IR-780@NPs L+ group, NP suspensions were irradiated with an 808 nm NIR laser (0.5 W cm^{-2}) for 5 min before incubating with cells. Subsequently, the cells were washed twice with DPBS and fixed with 4% paraformaldehyde (PFA) for 15 min. The resulting cells were stained with Hoechst 33342 and WGA-AF488, respectively. Fluorescence images were observed by CLSM (PE channel for DOX excited at 488 nm, FITC

channel for AF488 excited at 495 nm, and DAPI channel for Hoechst 33342 excited at 358 nm).

Cytotoxicity measurements

Cytotoxicity of DOX-loaded NPs was measured using the ATPLite-based assay. MCF-7 cells were seeded in 96-well plates at a density of 8×10^3 cells per well and cultured for 12 h. The cells were then incubated with different concentrations of DOX or DOX-loaded NPs (an equivalent DOX concentration of 0.3, 0.6, 1.2, 2.5, 5 and 10 μg mL^{-1}). For the IR-780@NPs group, the concentration of IR-780 was determined according to the DOX&IR-780@NPs group. The cells were incubated for 4 h and exposed under laser radiation (808 nm, 0.5 W cm^{-2}) for 5 min. After further incubation for 44 h, the supernatant was removed and an ATPlite stock solution (100 μL) was added to each well. The plates were shaken for 2 min before measuring with a plate reader.

Live/dead cell assay

MCF-7 cells were seeded in 24-well plates at a density of 1×10^5 cells per well and cultured for 12 h. The medium was removed and the cells were incubated with DOX or DOX-loaded NPs (an equivalent DOX concentration of 5 μg mL^{-1}). After incubation for 4 h, the supernatant was removed and 500 μL of fresh cell culture medium was added. Subsequently, the cells were exposed under laser radiation (808 nm, 0.5 W cm^{-2}) for 5 min. After incubation for 8 h, the medium was replaced with 500 μL of solution containing 2 μmol L^{-1} of Calcein-Am and 4 μmol L^{-1} of PI. After 10 min of incubation, fluorescence images were acquired using an inverted fluorescence microscope (ZEISS Axio Observer 3).

Tumor xenograft models

BALB/c mice (female, 5–6 weeks, 18–20 g) were purchased from Shanghai SLAC Laboratory Animal Co., Ltd (China). A xenograft tumor model was generated by injecting 2×10^6 of 4T1 cells in 100 μL of PBS into the right forelimb axilla of the BALB/c mice.[56] Animal studies were conducted following the regulations of the Animal Ethics Review Committee of Shandong University and the Health Guide for the Care and Use of Laboratory Animals of National Institutes.

In vivo imaging and biodistribution

In vivo imaging and biodistribution were performed by real-time NIRF imaging on the 4T1 tumor-bearing female BALB/c mice. Following tumor growth (approximately 300 mm^3), the mice were intravenously injected with free IR-780 (dissolved in an ethanol/water mixture with a volume ratio of 1 : 5) or IR-780@NPs (0.5 mg kg^{-1} of IR-780). At each predetermined time interval (2, 4, 8, 12, 24, and 48 h), the mice were anesthetized with isoflurane and observed using an IVIS Spectrum imaging system. After 12, 24, and 48 h post-injection, the mice were sacrificed, and the organs and tumors were harvested for further *ex vivo* evaluation.

In vivo antitumor activity

4T1 tumor-bearing female BALB/c mice were used to evaluate the antitumor efficacy *in vivo*. When the tumor volume was about 100 mm^3, animals were randomly separated into seven groups ($n = 5$). The mice received intravenous administrations of PBS, free DOX, free IR-780, DOX@NPs, IR-780@NPs, or DOX&IR-780@NPs with a DOX concentration of 5 mg kg^{-1}. After 24 h post-injection, the tumors for the groups of free IR-780 and DOX&IR-780@NPs were irradiated with the 1 W cm^{-2} NIR laser for 5 min. The mice in each group received a total of 3 administrations at 1, 3, and 7 days (total treatment duration of 18 days). Body weight, tumor volumes, and tumor weight were recorded at predetermined time points.

Immunohistochemical analysis

After 18 days of treatment, all the mice were sacrificed, and major organs (heart, liver, spleen, lungs and kidneys) and tumors were dissected for immunohistochemical analysis. All the organs and tumors were fixed in 4% PFA. Following dehydration and embedding in paraffin, the specimens were stained using H&E. Cell apoptosis of tumor tissues was assessed using the TUNEL assay. The slides were incubated with anti-Ki67 primary antibody and Rb IgG (H + L)/horseradish peroxidase secondary antibody for the evaluation of cell proliferation.

Statistical analysis

Statistical analyses were performed using the GraphPad software Prism (Version 6.01) using the two-sided Student's *t*-test.

Author contributions

Z. Gao, J. Hao and J. Cui conceived and designed the experiments; Z. Gao, W. Mu, Y. Tian, Y. Su and H. Sun performed the experiments; Z. Gao, W. Mu, N. Zhang and Y. Liu contributed to the animal experiments and analysis; G. Zhang, A. Li and D. Yu contributed to the MRI measurements; Z. Gao and J. Cui drafted the paper. All authors discussed the results and revised the manuscript.

Conflicts of interest

There are no conflicts to declare.

Acknowledgements

Notes and references

1 X. Ma, Y. Zhao and X. Liang, *Acc. Chem. Res.*, 2011, **44**, 1114–1122.

2 M. S. Bhojani, M. V. Dort, A. Rehemtulla and B. D. Ross, *Mol. Pharmaceutics*, 2010, **7**, 1921–1929.

3 E. K. Lim, T. Kim, S. Paik, S. Haam, Y. M. Huh and K. Lee, *Chem. Rev.*, 2015, **115**, 327–394.

4 C. Qi, J. Lin, L. H. Fu and P. Huang, *Chem. Soc. Rev.*, 2018, **47**, 357–403.

5 N. Ahmed, H. Fessi and A. Elaissari, *Drug Discovery Today*, 2012, **17**, 928–934.

6 Y. Ma, J. Huang, S. Song, H. Chen and Z. Zhang, *Small*, 2016, **12**, 4936–4954.

7 S. S. Kelkar and T. M. Reineke, *Bioconjugate Chem.*, 2011, **22**, 1879–1903.

8 C. Sun, J. S. Lee and M. Zhang, *Adv. Drug Delivery Rev.*, 2008, **60**, 1252–1265.

9 N. Lee, D. Yoo, D. Ling, M. H. Cho, T. Hyeon and J. Cheon, *Chem. Rev.*, 2015, **115**, 10637–10689.

10 M. Haris, S. K. Yadav, A. Rizwan, A. Singh, E. Wang, H. Hariharan, R. Reddy and F. M. Marincola, *J. Transl. Med.*, 2015, **13**, 313.

11 H. Wang, Y. Li, H. Bai, J. Shen, X. Chen, Y. Ping and G. Tang, *Adv. Funct. Mater.*, 2017, **27**, 1700339.

12 J. H. Lee, Y. M. Huh, Y. W. Jun, J. W. Seo, J. T. Jang, H. T. Song, S. Kim, E. J. Cho, H. G. Yoon, J. S. Suh and J. Cheon, *Nat. Med.*, 2007, **13**, 95–99.

13 J. W. Chen, M. Q. Sans, J. Alexei Bogdanov and R. Weissleder, *Radiology*, 2006, **240**, 473–481.

14 H. L. Chee, C. R. R. Gan, M. Ng, L. Low, D. G. Fernig, K. K. Bhakoo and D. Paramelle, *ACS Nano*, 2018, **12**, 6480–6491.

15 E. Y. Yu, P. Chandrasekharan, R. Berzon, Z. W. Tay, X. Y. Zhou, A. P. Khandhar, R. M. Ferguson, S. J. Kemp, B. Zheng, P. W. Goodwill, M. F. Wendland, K. M. Krishnan, S. Behr, J. Carter and S. M. Conolly, *ACS Nano*, 2017, **11**, 12067–12076.

16 J. Wahsner, E. M. Gale, A. Rodríguez-Rodríguez and P. Caravan, *Chem. Rev.*, 2019, **119**, 957–1057.

17 D. Kim, J. Kim, Y. Park, N. Lee and T. Hyeon, *ACS Cent. Sci.*, 2018, **4**, 324–336.

18 M. Mahmoudi, H. Hosseinkhani, M. Hosseinkhani, S. Boutry, A. Simchi, W. S. Journeay, K. Subramani and S. Laurent, *Chem. Rev.*, 2011, **111**, 253–280.

19 J. Pellico, C. M. Ellis and J. J. Davis, *Contrast Media Mol. Imaging*, 2019, 1845637.

20 J. Nicolas, S. Mura, D. Brambilla, N. Mackiewicz and P. Couvreur, *Chem. Soc. Rev.*, 2013, **42**, 1147–1235.

21 A. Kumari, S. K. Yadav and S. C. Yadav, *Colloids Surf., B*, 2010, **75**, 1–18.

22 J. K. Oh, R. Drumright, D. J. Siegwart and K. Matyjaszewski, *Prog. Polym. Sci.*, 2008, **33**, 448–477.

23 X. Xu, J. Wu, Y. Liu, P. E. Saw, W. Tao, M. Yu, H. Zope, M. Si, A. Victorious, J. Rasmussen, D. Ayyash, O. C. Farokhzad and J. Shi, *ACS Nano*, 2017, **11**, 2618–2627.

24 G. Gaucher, M. H. Dufresne, V. P. Sant, N. Kang, D. Maysinger and J. C. Leroux, *J. Controlled Release*, 2005, **109**, 169–188.

25 A. Blanazs, S. P. Armes and A. J. Ryan, *Macromol. Rapid Commun.*, 2009, **30**, 267–277.

26 C. Fetsch, J. Gaitzsch, L. Messager, G. Battaglia and R. Luxenhofer, *Sci. Rep.*, 2016, **6**, 33491.

27 X. B. Xiong, Z. Binkhathlan, O. Molavi and A. Lavasanifar, *Acta Biomater.*, 2012, **8**, 2017–2033.

28 J. Chen, J. Ding, Y. Wang, J. Cheng, S. Ji, X. Zhuang and X. Chen, *Adv. Mater.*, 2017, **29**, 1701170.

29 H. He, S. Ji, Y. He, A. Zhu, Y. Zou, Y. Deng, H. Ke, H. Yang, Y. Zhao, Z. Guo and H. Chen, *Adv. Mater.*, 2017, **29**, 1606690.

30 B. He, T. Tan, H. Wang, H. Hu, Z. Wang, J. Wang, J. Li, K. Sun, Z. Zhang and Y. Li, *Adv. Funct. Mater.*, 2018, **28**, 1705622.

31 J. Wang, S. Shen, D. Li, C. Zhan, Y. Yuan and X. Yang, *Adv. Funct. Mater.*, 2018, **28**, 1704806.

32 N. Qiu, X. Liu, Y. Zhong, Z. Zhou, Y. Piao, L. Miao, Q. Zhang, J. Tang, L. Huang and Y. Shen, *Adv. Mater.*, 2016, **28**, 10613–10622.

33 S. Wang, J. Lin, Z. Wang, Z. Zhou, R. Bai, N. Lu, Y. Liu, X. Fu, O. Jacobson, W. Fan, J. Qu, S. Chen, T. Wang, P. Huang and X. Chen, *Adv. Mater.*, 2017, **29**, 1701013.

34 X. Wang, J. Zhang, Y. Wang, C. Wang, J. Xiao, Q. Zhang and Y. Cheng, *Biomaterials*, 2016, **81**, 114–124.

35 V. A. Upadhyay and A. T. Fathi, *Curr. Opin. Hematol.*, 2018, **25**, 67–74.

36 Z. Li, S. Tan, S. Li, Q. Shen and K. Wang, *Oncol. Rep.*, 2017, **38**, 611–624.

37 J. Wang, Y. Liu, Y. Ma, C. Sun, W. Tao, Y. Wang, X. Yang and J. Wang, *Adv. Funct. Mater.*, 2016, **26**, 7516–7525.

38 X. Hu, Y. Zhang, Z. Xie, X. Jing, A. Bellotti and Z. Gu, *Biomacromolecules*, 2017, **18**, 649–673.

39 L. Su, R. Li, S. Khan, R. Clanton, F. Zhang, Y. N. Lin, Y. Song, H. Wang, J. Fan, S. Hernandez, A. S. Butters, G. Akabani, R. MacLoughlin, J. Smolen and K. L. Wooley, *J. Am. Chem. Soc.*, 2018, **140**, 1438–1446.

40 W. Chen, F. Meng, R. Cheng and Z. Zhong, *J. Controlled Release*, 2010, **142**, 40–46.

41 J. Zhou, Y. Wu, C. Wang, Q. Cheng, S. Han, X. Wang, J. Zhang, L. Deng, D. Zhao, L. Du, H. Cao, Z. Liang, Y. Huang and A. Dong, *Nano Lett.*, 2016, **16**, 6916–6923.

42 W. Fan, B. Yung, P. Huang and X. Chen, *Chem. Rev.*, 2017, **117**, 13566–13638.

43 Y. Zhong, C. Wang, L. Cheng, F. Meng, Z. Zhong and Z. Liu, *Biomacromolecules*, 2013, **14**, 2411–2419.

44 H. Gasmi, F. Danede, J. Siepmann and F. Siepmann, *J. Controlled Release*, 2015, **213**, 120–127.

45 W. Mu, D. Jiang, S. Mu, S. Liang, Y. Liu and N. Zhang, *ACS Appl. Mater. Interfaces*, 2019, **11**, 23591–23604.

46 X. Yu, C. Mu, D. Dai, X. Yuan, K. Zhang and L. Ren, *Macromol. Chem. Phys.*, 2016, **217**, 2700–2707.

47 I. Chikh Alard, J. Soubhye, G. Berger, M. Gelbcke, S. Spassov, K. Amighi, J. Goole and F. Meyer, *Polym. Chem.*, 2017, **8**, 2450–2456.

48 M. Döbbelin, V. Jovanovski, I. Llarena, L. J. Claros Marfil, G. Cabañero, J. Rodriguez and D. Mecerreyes, *Polym. Chem.*, 2011, **2**, 1275–1278.

49 Y. Chen, Z. Li, H. Wang, Y. Wang, H. Han, Q. Jin and J. Ji, *ACS Appl. Mater. Interfaces*, 2016, **8**, 6852–6858.

50 Y. Li, Q. Zhou, Z. Deng, M. Pan, X. Liu, J. Wu, F. Yan and H. Zheng, *Sci. Rep.*, 2016, **6**, 25968.

51 M. L. Viger, W. Sheng, K. Dore, A. H. Alhasan, C.-J. Carling, J. Lux, C. D. G. Lux, M. Grossman, R. Malinow and A. Almutairi, *ACS Nano*, 2014, **8**, 4815–4826.

52 F. Wang, Y.-C. Wang, S. Dou, M.-H. Xiong, T.-M. Sun and J. Wang, *ACS Nano*, 2011, **5**, 3679–3692.

53 J. Xiong, F. Meng, C. Wang, R. Cheng, Z. Liu and Z. Zhong, *J. Mater. Chem.*, 2011, **21**, 5786–5794.

54 H. Sun, B. Guo, R. Cheng, F. Meng, H. Liu and Z. Zhong, *Biomaterials*, 2009, **30**, 6358–6366.

55 Y. Mai and A. Eisenberg, *Chem. Soc. Rev.*, 2012, **41**, 5969–5985.

56 H. J. Li, J. Z. Du, X. J. Du, C. F. Xu, C. Y. Sun, H. X. Wang, Z. T. Cao, X. Z. Yang, Y. H. Zhu, S. Nie and J. Wang, *Proc. Natl. Acad. Sci. U. S. A.*, 2016, **113**, 4164–4169.